Available online at www.sciencedirect.com
SCIENCE DIRECT®
European Journal of Mechanics B/Fluids 24 (2005) 733–750

Numerical study around the corotational Maxwell model for the viscoelastic fluid flows

D. Sandri

LAN, Bât. 101, Université de Lyon 1, 69622 Villeurbanne cedex, France

Received 23 October 2003; received in revised form 11 February 2005; accepted 20 April 2005

Available online 17 May 2005

Abstract

We present numerical results for the FEM (finite element method) presented in [Comput. Methods Appl. Mech. Engrg. 191 (2002) 5045–5065]. This method is devoted to the approximation of fluid flows obeying the Oldroyd model. A particularity of this method, is to take into account the purely viscoelastic case, the so-called Maxwell model, important in practice. Numerical results are given for a fluid flowing in an abrupt plane 4 to 1 contraction. We use the corotational Maxwell model as benchmark in the choice of our computations. Results are also given for the upper convected Maxwell model. Interesting effects appear on the velocity profile: a phenomenon of quasi slip at the downstream wall.

Résumé

Nous présentons des résultats numériques pour la méthode d'éléments finis exposée dans [Comput. Methods Appl. Mech. Engrg. 191 (2002) 5045–5065]. Cette méthode permet de prendre en compte le cas purement viscoélastique du modèle de Maxwell. Pour guider nos calculs nous avons utilisé le modèle de Mawell corotationel, modèle qui présente des propriétés de stabilité numérique intéressantes. Nous observons des effets importants sur le profil de la vitesse : vitesse élevée près de la paroi en aval, avec quasiment un glissement et ceci dans le cadre de la contraction 4 en 1. Ces effets se produisent également dans le cas du modèle de Maxwell surconvecté, et ce, comme dans le cas précédent, pour des nombres de Weissenberg suffisamment grands.

Keywords: Finite element method; Viscoelastic flows

1. Introduction

We consider the following non-dimensional Oldroyd problem (cf. [1]) on a domain $\Omega \subset \mathbb{R}^2$ with polygonal boundary Γ:

$$(\mathcal{P}) \quad \begin{cases} \sigma + \lambda B(u,\sigma) = 2\alpha d(u) \quad \text{in } \Omega, \\ -\nabla\cdot\sigma - 2(1-\alpha)\nabla\cdot d(u) + \nabla p = f \quad \text{in } \Omega, \\ \nabla\cdot u = 0 \quad \text{in } \Omega, \\ u = u_0 \quad \text{on } \Gamma_1, \quad u\cdot n = 0 \quad \text{on } \Gamma_2 = \Gamma\backslash\Gamma_1, \\ \big[(\sigma + 2(1-\alpha)d(u) - pI)\cdot n\big]\cdot t = 0 \text{ on } \Gamma_2, \\ \sigma = \sigma_0 \quad \text{on } \Gamma^-, \end{cases}$$

E-mail address: dsandri@maply.univ-lyon1.fr (D. Sandri).

0997-7546/$ – see front matter
doi:10.1016/j.euromechflu.2005.04.004

where B is given by the objective derivative

$$B(u,\sigma) = u\cdot\nabla\sigma + \sigma\omega(u) - \omega(u)\sigma - a\big(d(u)\sigma + \sigma d(u)\big),$$

with $f \in [L^2(\Omega)]^2$, $u_0 \in [H^1(\Omega)]^2$, $\sigma_0 \in [L^2(\Gamma^-)]^4$ where $\Gamma^- = \{x \in \Gamma,\ \lambda n\cdot u_0(x) < 0\}$ is the inflow section of the boundary (for $\lambda = 0$, we then have $\Gamma^- = \emptyset$), n is the outward unit normal vector on Γ, t the unit tangent, and $n\cdot u_0$ the scalar product of n and u_0. We denote by Γ_1 a subset, with positive measure, of the boundary Γ. Let ds be the measure on the boundary Γ, we assume that the compatibility conditions $\int_{\Gamma_1} u_0\cdot n\,ds = 0$ and $u_0\cdot n = 0$ on Γ_2 are satisfied (it is not necessary that u_0 has divergence zero). We assume that the extra-stress tensors σ and σ_0 are symmetric, u is the velocity vector and p is the pressure. We shall assume that α, λ and a are parameters such that $0 < \alpha \leqslant 1$, $\lambda \geqslant 0$ and $a \in [-1, 1]$.

We have denoted for tensors σ, $\nabla\cdot\sigma = \sigma_{ij,j}$ the divergence of σ, with the Einstein summation convention, $\sigma : \tau$ the sum $\sigma_{ij}\tau_{ij}$, $\nabla\cdot u = u_{i,i}$ the divergence of u, $u\cdot\nabla\sigma = u_k\sigma_{ij,k}$, $\nabla p = p_{,i}$ the gradient of p, $d(u) = \frac{1}{2}(u_{i,j} + u_{j,i})$ the rate of strain tensor of u et $\omega(u) = \frac{1}{2}(u_{i,j} - u_{j,i})$ the vorticity tensor of u.

In the sequel, we denote by $(\ ,\ )$ the scalar product on $[L^2(\Omega)]^n$, $n \in \mathbb{N}$, and we denote by $|\cdot|$ the corresponding norm. For a section ℓ of Γ we denote by $\langle\ ,\ \rangle_\ell$ the scalar product $\langle\sigma,\tau\rangle_\ell = \int_\ell \sigma : \tau|u_0\cdot n|\,ds$.

For $\alpha = 1$, this problem is also called the Maxwell problem. The corotational Oldroyd model (called the corotational Maxwell model when $\alpha = 1$) is given for $a = 0$ and the upper convected Oldroyd model (called the upper convected Maxwell model, if $\alpha = 1$) is given for $a = 1$. If we denote η_p the polymeric viscosity and η_s the solvent viscosity, α is then the viscoelastic fraction of the viscosity:

$$\alpha = \frac{\eta_p}{\eta_p + \eta_s}$$

and $(1-\alpha)$ the Newtonian fraction of the viscosity. The case $\alpha = 1$ or α close to 1 is important because in many cases the solvent is, for all practical purposes, absent. In the network theory, $1-a$ is a "slip constant" introduced to relax the affine motion assumption (see [1], vol. II, p. 374). Especially, this constant allows to predict non-zero second-normal-stress difference. As quoted in ([1], vol. II, p. 376) : "Experimental data on polymer melts and concentrated solutions suggest a value of" a in $]0.5, 0.9[$.

We have chosen the corotational model as a vital lead because this model presents the advantage to provide a priori estimates properties. This is due to the relation

$$\big(\sigma\omega(u) - \omega(u)\sigma\big) : \sigma = 0 \tag{1.1}$$

which leads to a priori estimates. For example this property is used in [2] to obtain the convergence of a FE element method for the approximation of a linearized version of the Maxwell model.

For the fixed point method used to solve the FEM problem which is considered below, it appears that these properties lead to results of convergence for relatively high values of λ. The convergence is linear and, compared to the upper-convected Maxwell case, more rapid. The solutions obtained are numerically of good quality and they are generally without oscillations. Furthermore, all the computational process is relatively robust when we refine the mesh in a sufficiently regular manner, or when we use thinner meshes. For these reasons, we use this model as a guideline in the choice of the meshes, of the parameters of the FEM method, of the iterative method, etc. Notably, for sufficiently high Weissenberg number there appears a phenomenon of "quasi-slip" of the velocity along the wall of the downstream section of the contraction. We have used the term quasi-slip in the sense that, up to numerical error, the fluid slips at the wall, with, however, a no-slip boundary condition.

The numerical study of the corotational case is then extended to the upper convected case. The quasi-slip for the velocity persists but an oscillating component σ_{11} of the tensor σ appears at the downstream wall. It seems to be a consequence of the convection of σ by a velocity u having small oscillations at the downstream wall. These oscillations have a tendency to disappear when we use a thinner and more regular mesh.

The outline of the paper is as follows: in Section 2 we present the FEM used in this paper. In Section 3, we describe numerical results obtained for the abrupt 4 to 1 contraction. We study the corotational case in Section 3.1 and the upper convected case in Section 3.2. The influence of the refinement of mesh on the solutions is studied in Section 3.3. Finally, in Section 3.4 we discuss about the appearance of the quasi-slip, notably its links with the Poiseuille flow.

2. The FEM approximation of $(\mathcal{P})$

Let $T = \{\tau, \tau \in [H^1(\Omega)]^4,\ \tau \text{ symmetric}\}$, the tensor space, $X = \{u \in [H^1(\Omega)]^2, u = 0 \text{ on } \Gamma_1,\ u\cdot n = 0 \text{ on } \Gamma_2\}$ and $M = L^2_0(\Omega) = \{q \in L^2(\Omega),\ (1,q) = 0\}$ the space of pressures with zero mean value. We remark that for the Stokes Problem obtained with $\lambda = 0$ in $(\mathcal{P})$, the natural choice for the tensor space T is $[L^2(\Omega)]^4_s$ (s for symmetric), in fact the choice of the space T above is made only in view of discretization.

We denote by $\{T_h \times X_h \times M_h \subset T \times X \times M\}_{h>0}$ a family of FE spaces where h is a discretization parameter (in practice, h will be the size of the mesh). With this choice of T, B is then well defined on $X \times T$.

As in the approximation of the Stokes problem we shall assume that the following velocity–pressure condition holds:

$$\inf_{q\in M_h}\sup_{v\in X_h}\frac{(\nabla\cdot v,q)}{|d(v)||q|}\geqslant\beta>0, \tag{2.1}$$

with β independent of h.

Now, we give the formulation $(\mathcal{Q})$ considered in this paper. Some details to obtain this formulation are given in [2] and also in [3] where boundaries conditions and a δ-dependent mesh version are studied (δ is an upwinding parameter) and also in [4] for a numerical study of this method.

The constitutive equation is approximated with a method of SUPG (Streamline Upwind Petrov Galerkin) type. We have chosen an upwinding of the kind $\tau+\delta\lambda B(u,\tau)$, with $\delta>0$.

Let μ be a parameter, the problem, obtained by introducing a fraction $1-\theta$ ($\theta\in]0,1]$) of the constitutive equation in the momentum equation is then:

Find $(\sigma,u,p)\in T\times(u_0+X)\times M$ *such that* $\forall(\tau,v,q)\in T\times X\times M$ *we have*:

$$(\mathcal{Q})\quad\begin{cases}\big(\sigma+\lambda B(u,\sigma),\tau+\delta\lambda B(u,\tau)\big)+\lambda(1+\delta)\langle\sigma,\tau\rangle_{\Gamma^-}=2\alpha\big(d(u),\tau+\delta\lambda B(u,\tau)\big)+\lambda(1+\delta)\langle\sigma_0,\tau\rangle_{\Gamma^-},\\ \theta\big(\sigma,d(v)\big)+(1-\theta)\big(2\alpha d(u)-\lambda B(u,\sigma),d(v)\big)+2(1-\alpha)\big(d(u),d(v)\big)-(p,\nabla\cdot v)+\mu(\nabla\cdot u,\nabla\cdot v)=(f,v),\\ (\nabla\cdot u,q)=0,\end{cases}$$

and its corresponding approximation:

Find $(\sigma_h,u_h,p_h)\in T_h\times(u_0+X_h)\times M_h$ *such that* $\forall(\tau,v,q)\in T_h\times X_h\times M_h$ *we have*:

$$(\mathcal{Q}_h)\quad\begin{cases}\big(\sigma_h+\lambda B(u_h,\sigma_h),\tau+\delta\lambda B(u_h,\tau)\big)+\lambda(1+\delta)\langle\sigma_h,\tau\rangle_{\Gamma^-}=2\alpha\big(d(u_h),\tau+\delta\lambda B(u_h,\tau)\big)+\lambda(1+\delta)\langle\sigma_0,\tau\rangle_{\Gamma^-},\\ \theta\big(\sigma_h,d(v)\big)+(1-\theta)\big(2\alpha d(u_h)-\lambda B(u_h,\sigma_h),d(v)\big)+2(1-\alpha)\big(d(u_h),d(v)\big)-(p_h,\nabla\cdot v)\\ \qquad+\mu(\nabla\cdot u_h,\nabla\cdot v)=(f,v),\\ (\nabla\cdot u_h,q)=0.\end{cases}$$

In [2], a key to obtain some results of convergence, including the Maxwell linearized problem, is to select $\mu>0$ and to pick

$$\theta=\frac{1}{1+\delta}$$

in the formulation.

In this paper, the iterative method used to solve problem $(\mathcal{Q}_h)$ is the following implicit scheme. Let $(\sigma_h^n,u_h^n,p_h^n)\in T_h\times(u_0+X_h)\times M_h$ be given, $(\sigma_h^{n+1},u_h^{n+1},p_h^{n+1})\in T_h\times(u_0+X_h)\times M_h$ is then given by:

$$(\mathcal{FP})\quad\begin{cases}\big(\sigma_h^{n+1}+\lambda B\big(u_h^n,\sigma_h^{n+1}\big),\tau+\delta\lambda B\big(u_h^n,\tau\big)\big)+\lambda(1+\delta)\big\langle\sigma_h^{n+1},\tau\big\rangle_{\Gamma^-}\\ \qquad=2\alpha\big(d\big(u_h^{n+1}\big),\tau+\delta\lambda B\big(u_h^n,\tau\big)\big)+\lambda(1+\delta)\langle\sigma_0,\tau\rangle_{\Gamma^-},\\ \theta\big(\sigma_h^{n+1},d(v)\big)+(1-\theta)\big(2\alpha d\big(u_h^{n+1}\big)-\lambda B\big(u_h^n,\sigma_h^{n+1}\big),d(v)\big)\\ \qquad+2(1-\alpha+c)\big(d\big(u_h^{n+1}\big),d(v)\big)-\big(p_h^{n+1},\nabla\cdot v\big)+\mu\big(\nabla\cdot u_h^{n+1},\nabla\cdot v\big)=(f,v)+2c\big(d\big(u_h^n\big),d(v)\big),\\ \big(\nabla\cdot u_h^{n+1},q\big)=0,\ \forall(\tau,v,q)\in T_h\times X_h\times M_h.\end{cases}$$

The c term allows us to improve, in certain cases and in a very significant manner, the convergence of the fixed point algorithm above (this c term is considered in [5], a numerical study relating c to the convergence of $(\mathcal{FP})$ is carried out in [4]). In this paper we shall use values such as $c=0$, $c=\frac{1}{4}$, $c=\frac{1}{2}$.

In all the numerical tests of the following Section 3, we shall select (σ_h^0,u_h^0,p_h^0) to be the solution of the problem $(\mathcal{Q}_h)$ with $\lambda=0$ in the equations. We remark that (σ_h^0,u_h^0,p_h^0) is then an approximation of the solution of a Stokes problem.

In view of studying the error and the convergence order of the iterative method $(\mathcal{FP})$, we shall use the following energy norm:

$$\big\|(\sigma,u,p)\big\|=\big[|\sigma|^2+\big|d(u)\big|^2+|p|^2\big]^{1/2}.$$

In the iterative procedure we observe after some iterations a convergence of the kind:

$$\left\|\left(\sigma_h^n, u_h^n, p_h^n\right) - \left(\sigma_h^{n-1}, u_h^{n-1}, p_h^{n-1}\right)\right\| \leqslant A\gamma^n.$$

We give an estimate of the ratio of convergence γ by studying, for $n \geqslant 2$, the difference

$$\left\|\left(\sigma_h^n, u_h^n, p_h^n\right) - \left(\sigma_h^{n-1}, u_h^{n-1}, p_h^{n-1}\right)\right\|$$

in log-scale.

In this paper we use the following finite element spaces. The domain Ω is equipped with a conforming triangulation $\{\mathcal{T}_h\}_{h>0}$ of triangles K. The pair (u, p) is approximated using the Taylor–Hood FE which satisfies (2.1) and the tensor σ is approximated with a P_1 continuous approximation. Then we select:

$$T_h = \left\{\tau \in T;\ \tau|_K \in \left[P_1(K)\right]^4,\ \forall K \in \mathcal{T}_h\right\},$$
$$M_h = \left\{q \in M \cap \mathcal{C}^0(\overline{\Omega});\ q|_K \in P_1(K),\ \forall K \in \mathcal{T}_h\right\},$$
$$X_h = \left\{v \in X;\ v|_K \in \left[P_2(K)\right]^2,\ \forall K \in \mathcal{T}_h\right\},$$

where $P_1(K) = \{v : K \to \mathbb{R},\ v(x, y) = \alpha + \beta x + \gamma y,\ (\alpha, \beta, \gamma) \in \mathbb{R}^3\}$ and $P_2(K) = \{v : K \to \mathbb{R},\ v(x, y) = \alpha + \beta x + \gamma y + \delta xy + \epsilon x^2 + \phi y^2,\ (\alpha, \beta, \gamma, \delta, \epsilon, \phi) \in \mathbb{R}^6\}$. With the boundary conditions selected for the velocity (Poiseuille type flow), we can choose in our computations $u_0 \in U_h = \{v \in [\mathcal{C}^0(\overline{\Omega})]^2;\ v|_K \in [P_2(K)]^2,\ \forall K \in \mathcal{T}_h\}$. With this choice, the solution u_h of problem $(\mathcal{Q}_h)$ belongs to $u_0 + X_h = \{v_h \in U_h,\ v_h = u_0 \text{ on } \Gamma_1\}$, thus u_h is P_2 on each triangle.

3. Numerical study of the abrupt contraction

We consider the test problem of a fluid flowing in an abrupt 4 to 1 plane contraction, with domain of length 16 delimited by the vertices $(0, 0)$, $(16, 0)$, $(16, 1)$ $(8, 1)$, $(8, 4)$, $(0, 4)$ (see Fig. 1). We set $\Gamma_1 = \Gamma \backslash \{(x, y) \in \Gamma,\ y = 0\}$, $\Gamma_2 = \{(x, y) \in \Gamma,\ y = 0\}$ and $\Gamma^- = \{(x, y) \in \Gamma,\ x = 0\}$.

We select the body force as $f = 0$, the Dirichlet conditions for u_1 are chosen as follows:

- At the inflow boundary: $u_1(0, y) = 1 - y^2/16$, $y \in [0, 4]$,
- At the outflow boundary: $u_1(16, y) = 4 - 4y^2$, for $y \in [0, 1]$,

on the remainder of Γ_1 we select $u_1 = 0$ i.e.:

- $u_1(x, 4) = 0$, for $x \in [0, 8]$,
- $u_1(8, y) = 0$, for $y \in [1, 4]$,
- $u_1(x, 1) = 0$, for $x \in [8, 16]$.

For u_2, we select $u_2 = 0$ on Γ_1, therefore the condition $u \cdot n = 0$ on Γ_2 leads to

- $u_2 = 0$ on Γ.

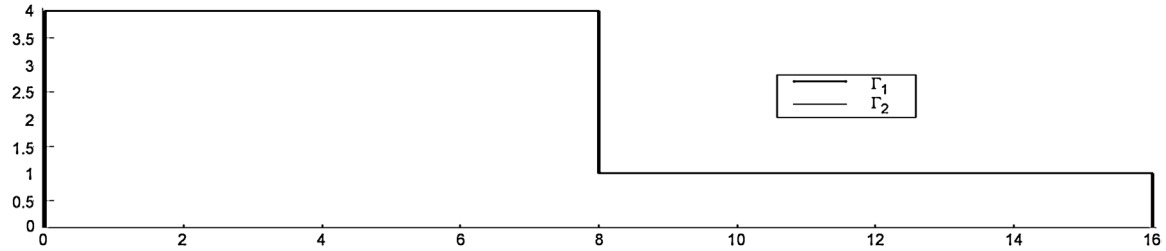

Fig. 1. Geometry of the 4 to 1 contraction.

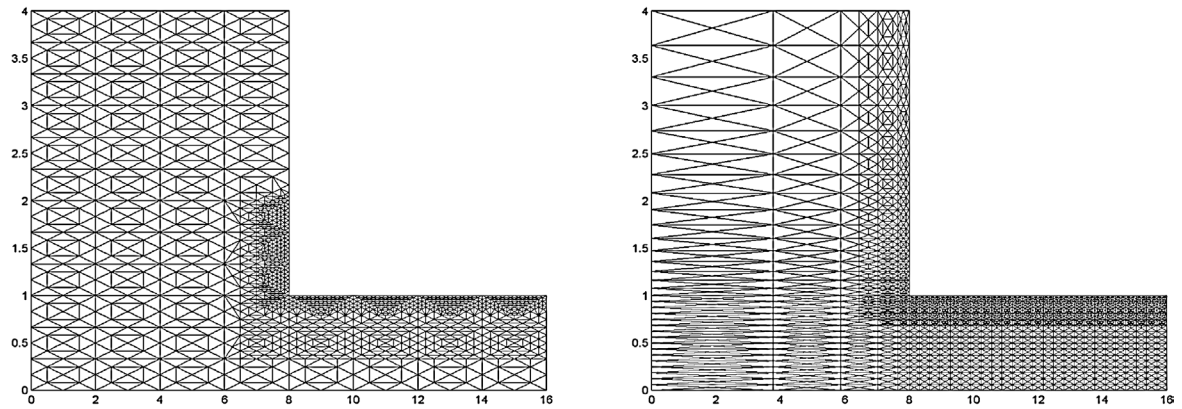

Fig. 1a. Meshes $\mathcal{M}_1$, $\mathcal{M}_2$.

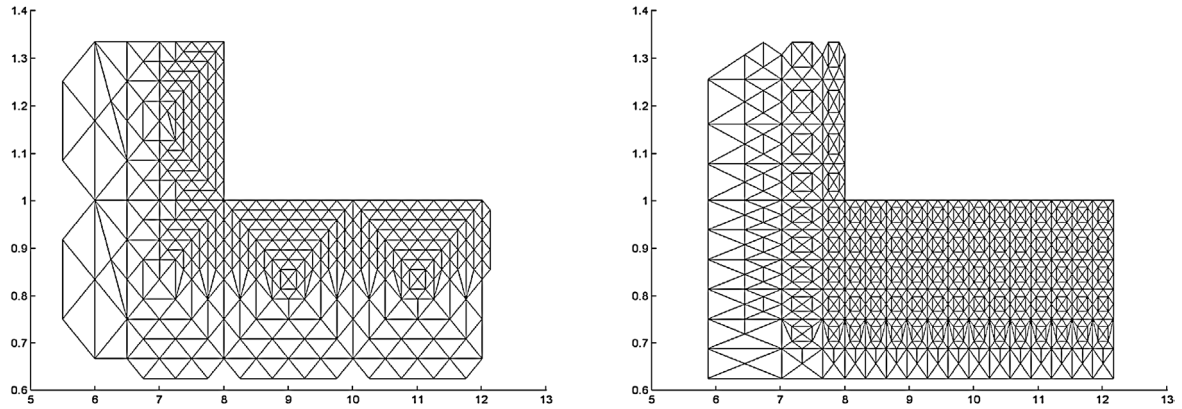

Fig. 1b. Meshes $\mathcal{M}_1$, $\mathcal{M}_2$.

At the downstream wall we then have for the shear stress $\dot{\gamma} = |u_{1,2}(16, 1)| = 8$ and the Weissenberg number is then usually defined for this flow as $We = \lambda\dot{\gamma} = 8\lambda$.

The inflow boundary condition upon σ is chosen as the value of $\tilde{\sigma}(0, y)$, $\tilde{\sigma}$ being defined as follows. For the upper convected model we choose $\tilde{\sigma}$ as the solution of the Poiseuille flow on $\mathbb{R} \times [-4, 4]$. This gives

$$\sigma_{11}(0, y) = 2\lambda\alpha u_{1,2}^2(0, y), \qquad \sigma_{12}(0, y) = \alpha u_{1,2}(0, y), \qquad \sigma_{22}(0, y) = 0.$$

In the corotational case ($a = 0$) we select for $\tilde{\sigma}$ the solution independent of x which satisfies on $\mathbb{R} \times [-4, 4]$ the constitutive equation

$$\tilde{\sigma} + \lambda\big(\tilde{u} \cdot \nabla\tilde{\sigma} + \tilde{\sigma}\omega(\tilde{u}) - \omega(\tilde{u})\tilde{\sigma} - a\big(d(\tilde{u})\tilde{\sigma} + \tilde{\sigma}d(\tilde{u})\big)\big) = 2\alpha d(\tilde{u}),$$

with $\tilde{u}(x, y) = 1 - y^2/16$. This gives:

$$\sigma_{11}(0, y) = \frac{\lambda\alpha(1 + a)u_{1,2}^2(0, y)}{1 + \lambda^2(1 - a^2)u_{1,2}^2(0, y)}, \qquad \sigma_{12}(0, y) = \frac{\alpha u_{1,2}(0, y)}{1 + \lambda^2(1 - a^2)u_{1,2}^2(0, y)},$$

$$\sigma_{22}(0, y) = \frac{-\lambda(1 - a)\alpha u_{1,2}^2(0, y)}{1 + \lambda^2(1 - a^2)u_{1,2}^2(0, y)}.$$

Let $\sigma_{\text{tot}} = (\sigma + 2(1 - \alpha)d(u) - pI)$ be the stress tensor. In order to study the influence of the outflow boundary conditions we have also tested other outflow boundary conditions as $(\sigma_{\text{tot}} \cdot n) \cdot n = 0$ and $u \cdot t = 0$ (fully developed profile) or $\sigma_{\text{tot}} \cdot n = 0$ without conditions on u. With these conditions, computations show that the solutions keep a similar behaviour (except at the exit

of the channel for x close to 16). In Section 3.4, in the Poiseuille flow case, we present computations made with the condition $\sigma_{\text{tot}} \cdot n = 0$ at the outflow boundary. For these conditions, we notice that the space of pressures is then given by $M = L^2(\Omega)$.

The computations are made on two meshes given in Fig. 1a: mesh $\mathcal{M}_1$ and mesh $\mathcal{M}_2$ which is thinner near the wall $y = 1$. A zoom of these meshes is given in Fig. 1b. The number of nodes of the triangulation is resp. 1221 and 2266, the number of faces is resp. 2310 and 4358, and the number of unknowns is resp. 14 385 and 26 841. The CPU time used for each step of the iterative method ($\mathcal{FP}$) is, on average, resp. 92 s and 280 s (for a processor at 1500 GHz).

The coordinates of the triangle located at the re-entrant corner, with an edge on the wall $y = 1$, are resp. about $(8, 1)$, $(8.125, 0.979)$, $(8.25, 1)$ for the first mesh and $(8, 1)$, $(8.08, 0.984)$, $(8.16, 1)$ for the second mesh. Fig. 1b shows that the second mesh is thinner and more regular that the first mesh in the upstream section of the contraction. In the upstream section of $\mathcal{M}_2$, for $x \lesssim 6$, we notice that we use relatively flat triangles. Since the flatness of triangles in a mesh can reduce the accuracy of the FEM, we have also tested, in $\mathcal{M}_1$, triangles which are less flat. However, we have checked that $\mathcal{M}_1$ and $\mathcal{M}_2$ give similar solutions for $x \lesssim 6$.

3.1. Simulations with the mesh $\mathcal{M}_1$: the corotational case

For the mesh $\mathcal{M}_1$ and the corotational case we have studied the three following cases:

- Case 3.1.1: $We = 8\lambda = 0.4$, with $\alpha = 1$ (Figs. 2–4);
- Case 3.1.2: $We = 8\lambda = 1$, with $\alpha = \frac{8}{9}$ (Figs. 5–7);
- Case 3.1.3: $We = 8\lambda = 1$, with $\alpha = 1$ (Figs. 8–10).

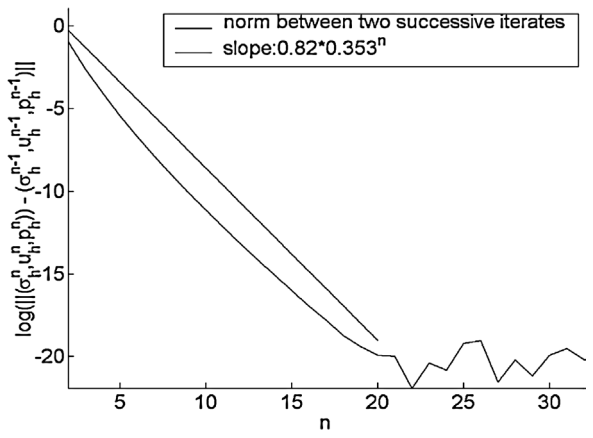

Fig. 2. Ratio of convergence. Case 3.1.1. Mesh $\mathcal{M}_1$, $a = 0$, $We = 8\lambda = 0.4$, $\alpha = 1$, $\theta = \frac{5}{6}$, $\delta = \frac{1}{5}$, $c = 0$, $\mu = 2$.

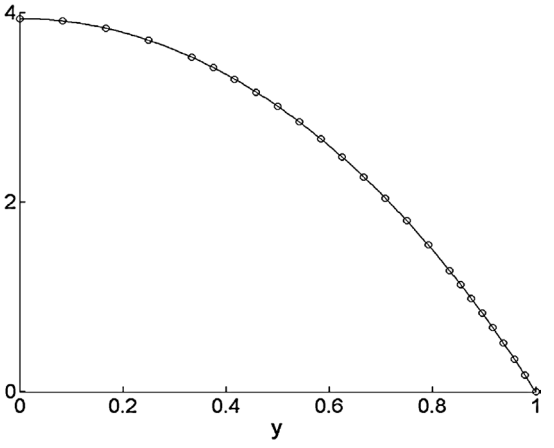

Fig. 3. u_1 on the line $x = 12$. Case 3.1.1. Mesh $\mathcal{M}_1$, $a = 0$, $We = 8\lambda = 0.4$, $\alpha = 1$, $\theta = \frac{5}{6}$, $\delta = \frac{1}{5}$, $c = 0$, $\mu = 2$.

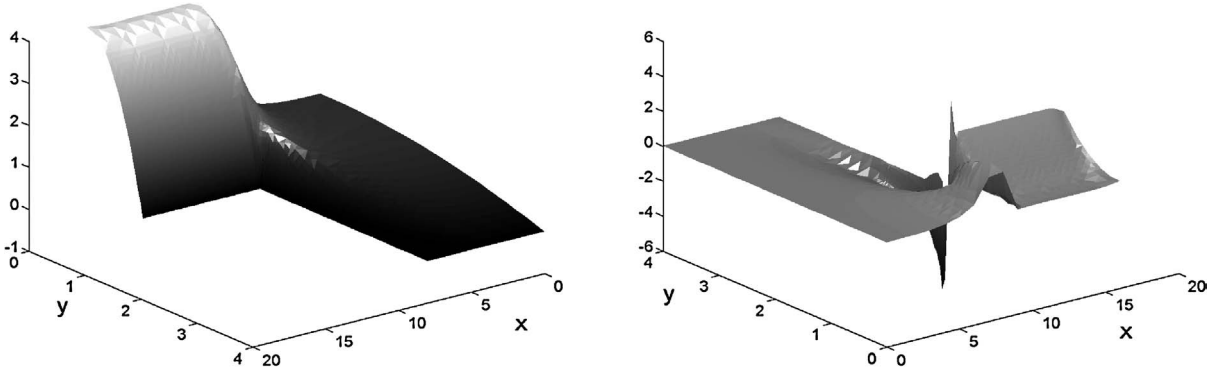

Fig. 4. Graph of u_1 (reverse angle) and σ_{11}. Case 3.1.1 (continuation). Mesh $\mathcal{M}_1$, $a = 0$, $We = 8\lambda = 0.4$, $\alpha = 1$, $\theta = \frac{5}{6}$, $\delta = \frac{1}{5}$, $c = 0$, $\mu = 2$.

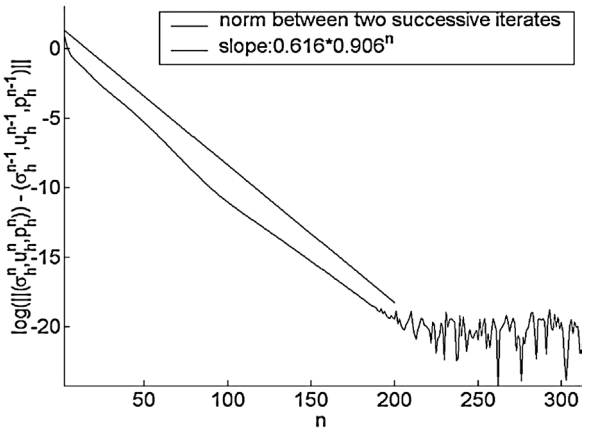

Fig. 5. Ratio of convergence. Case 3.1.2. Mesh $\mathcal{M}_1$, $a = 0$, $We = 8\lambda = 1$, $\alpha = \frac{8}{9}$, $\theta = \frac{5}{6}$, $\delta = \frac{1}{5}$, $c = 0$, $\mu = 2$.

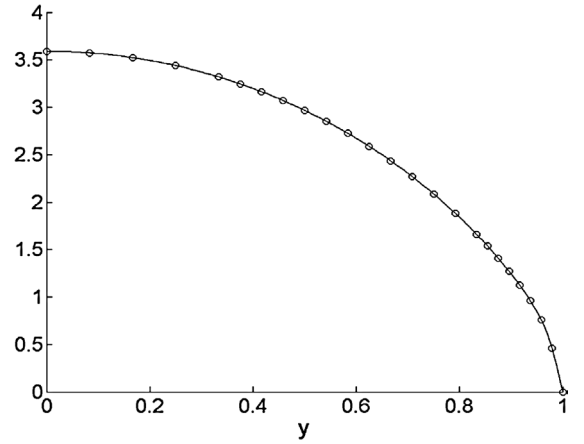

Fig. 6. u_1 on the line $x = 12$. Case 3.1.2. Mesh $\mathcal{M}_1$, $a = 0$, $We = 8\lambda = 1$, $\alpha = \frac{8}{9}$, $\theta = \frac{5}{6}$, $\delta = \frac{1}{5}$, $c = 0$, $\mu = 2$.

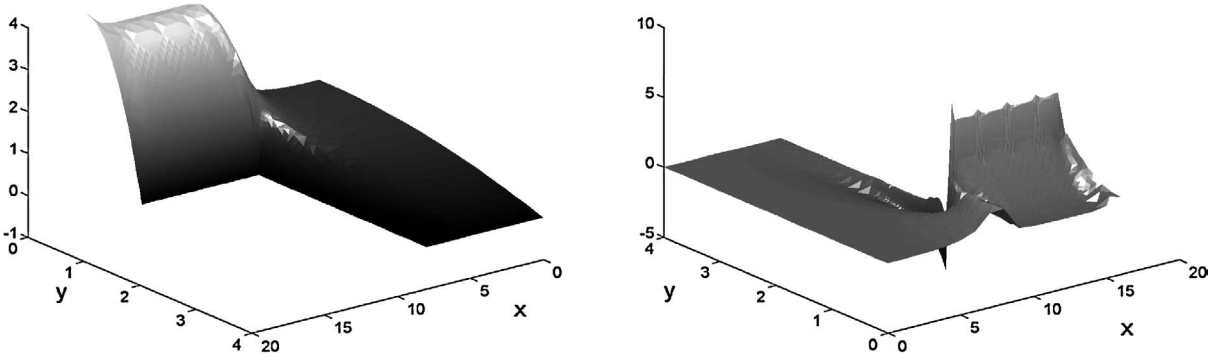

Fig. 7. Graph of u_1 (reverse angle) and σ_{11}. Case 3.1.2 (continuation). Mesh $\mathcal{M}_1$, $a = 0$, $We = 8\lambda = 1$, $\alpha = \frac{8}{9}$, $\theta = \frac{5}{6}$, $\delta = \frac{1}{5}$, $c = 0$, $\mu = 2$.

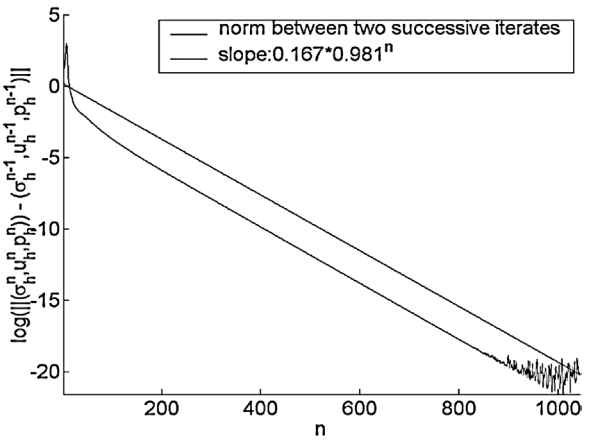

Fig. 8. Ratio of convergence. Case 3.1.3. Mesh $\mathcal{M}_1$, $a = 0$, $We = 8\lambda = 1$, $\alpha = 1$, $\theta = \frac{5}{6}$, $\delta = \frac{1}{5}$, $c = 0$, $\mu = 2$.

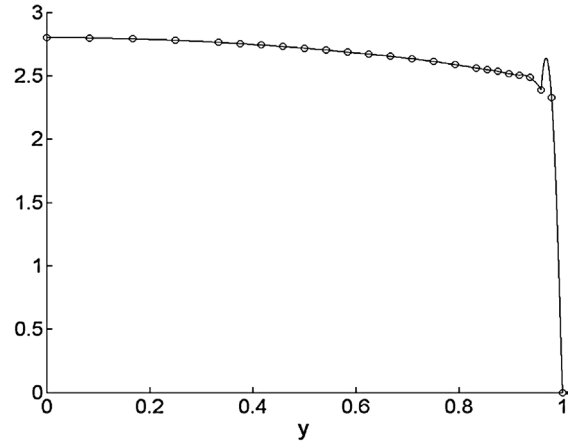

Fig. 9. u_1 on the line $x = 12$. Case 3.1.3. Mesh $\mathcal{M}_1$, $a = 0$, $We = 8\lambda = 1$, $\alpha = 1$, $\theta = \frac{5}{6}$, $\delta = \frac{1}{5}$, $c = 0$, $\mu = 2$.

The parameters chosen are $\delta = \frac{1}{5}$, $\theta = \frac{5}{6}$ and $c = 0$. The curves of the ratio of convergence, the graphics for u_1 and σ_{11} are given in Figs. 2–10. For 2D representations of the velocity, the circles indicate the degrees of freedom of the P_2 element (as in Fig. 3), these degrees of freedom being located at the vertices and at the mid-points of the edges of the triangles of the mesh. In

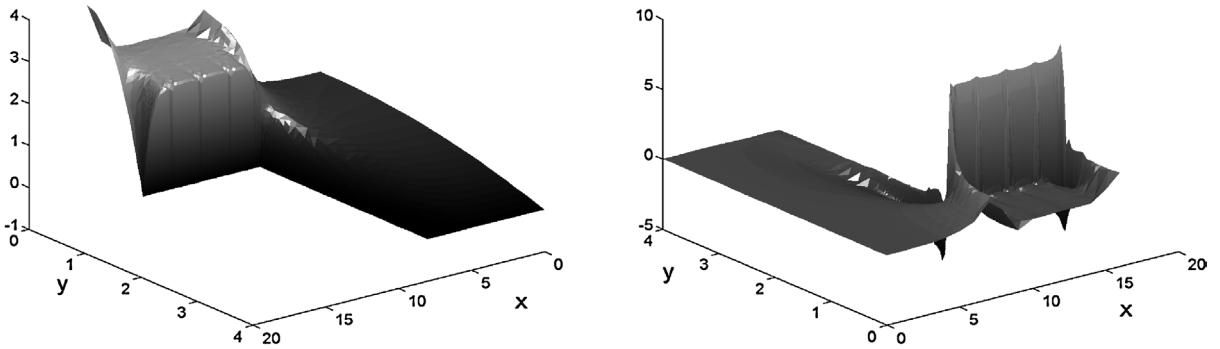

Fig. 10. Graph of u_1 (reverse angle) and σ_{11}. Case 3.1.3 (continuation). Mesh $\mathcal{M}_1$, $a = 0$, $We = 8\lambda = 1$, $\alpha = 1$, $\theta = \frac{5}{6}$, $\delta = \frac{1}{5}$, $c = 0$, $\mu = 2$.

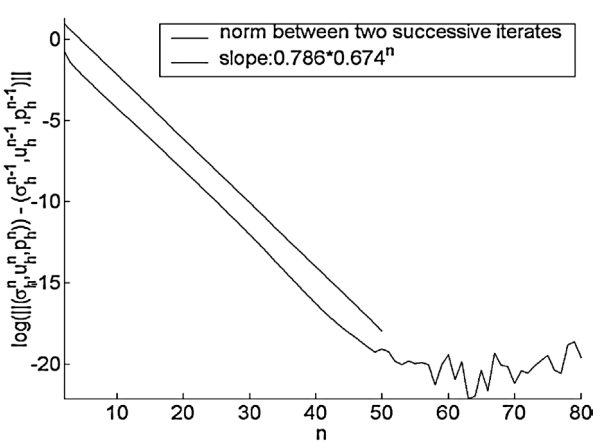

Fig. 11. Ratio of convergence. Case 3.2.1. Mesh $\mathcal{M}_1$, $a = 1$, $We = 8\lambda = 0.8$, $\alpha = 1$, $\theta = \frac{5}{6}$, $\delta = \frac{1}{5}$, $c = 0$, $\mu = 2$.

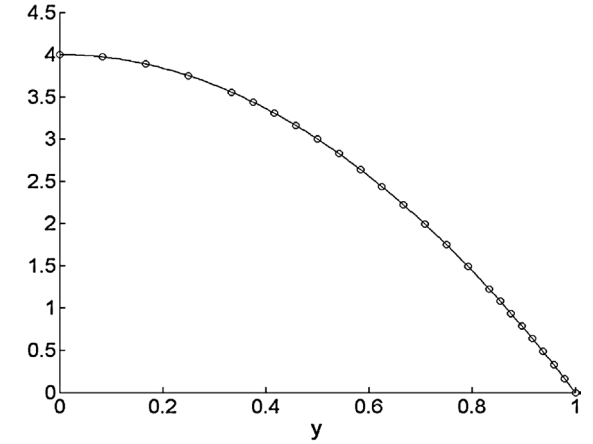

Fig. 12. u_1 on the line $x = 12$. Case 3.2.1. Mesh $\mathcal{M}_1$, $a = 1$, $We = 8\lambda = 0.8$, $\alpha = 1$, $\theta = \frac{5}{6}$, $\delta = \frac{1}{5}$, $c = 0$, $\mu = 2$.

our graphs below, the vertices alternate with the mid-points. For 3D representations of u we have plotted the P_1 interpolate of u at the nodes of the mesh (as in Fig. 4), with a viewpoint opposite to the usual viewpoint.

In Figs. 2, 5 and 8, we see that the iterative method gives linear convergence. In the first case 3.1.1, we observe in Figs. 3 and 4 that the first component of the velocity is relatively close to the solution of the Stokes problem.

In the second case 3.1.2, we notice the same situation but, at the downstream section, the profile of u_1 becomes flatter (see Figs. 6 and 7).

In the third case 3.1.3, for the Maxwell model (i.e. $\alpha = 1$) with $We = 1$, we remark, at the wall $y = 1$, an important change for the profile of the first component of the velocity (see Figs. 9 and 10). In this third case we observe that the choice of a sufficiently high Weissenberg number in the corotational Maxwell model leads to a quasi-slip phenomenon at the downstream wall. On Fig. 9 we have near the wall the values $u_1(12, 0.958) = 2.39$ and $u_1(12, 0.979) = 2.33$.

3.2. Simulations with the mesh $\mathcal{M}_1$: the upper convected case

For the mesh $\mathcal{M}_1$ and the upper convected case we have studied the two following cases:

- Case 3.2.1: $We = 8\lambda = 0.8$ with $\alpha = 1$ (Figs. 11–13);
- Case 3.2.2: $We = 8\lambda = 1$ with $\alpha = 1$ (Figs. 14–16).

We select for the parameters of the FE method $\delta = \frac{1}{5}$ and $\theta = \frac{5}{6}$, we use in the iterative method $c = 0$ in the first case and $c = \frac{1}{4}$ in the second case. The results are described in Figs. 11–16. In the first case 3.2.1, the results are of the same order as those of the literature (a discussion concerning the results of the literature and the method of this paper is developed in [4]).

Now, in the second case 3.2.2, we observe that the phenomenon of a quasi-slip for the velocity appears again for $We = 1$ (see Figs. 15 and 16). On Fig. 15, u_1 take the values $u_1(12, 0.958) = 2.40$ and $u_1(12, 0.979) = 2.30$. Moreover, we remark that

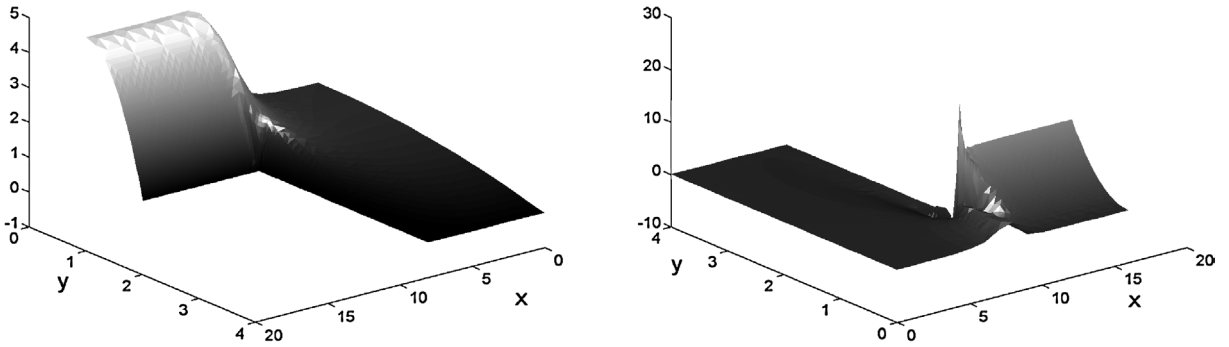

Fig. 13. Graph of u_1 (reverse angle) and σ_{11}. Case 3.2.1 (continuation). Mesh $\mathcal{M}_1$, $a = 1$, $We = 8\lambda = 0.8$, $\alpha = 1$, $\theta = \frac{5}{6}$, $\delta = \frac{1}{5}$, $c = 0$, $\mu = 2$.

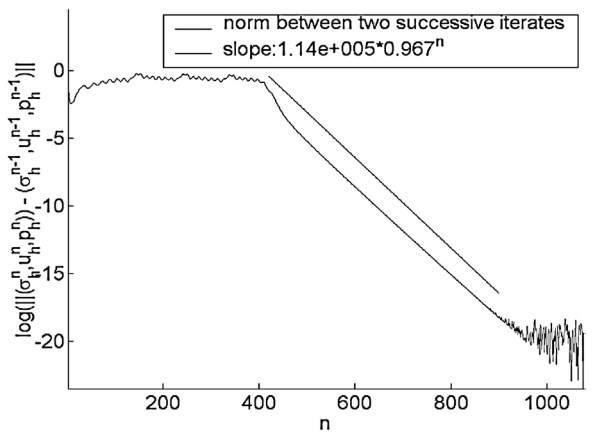

Fig. 14. Ratio of convergence. Case 3.2.2. Mesh $\mathcal{M}_1$, $a = 1$, $We = 8\lambda = 1$, $\alpha = 1$, $\theta = \frac{5}{6}$, $\delta = \frac{1}{5}$, $c = \frac{1}{4}$, $\mu = 2$.

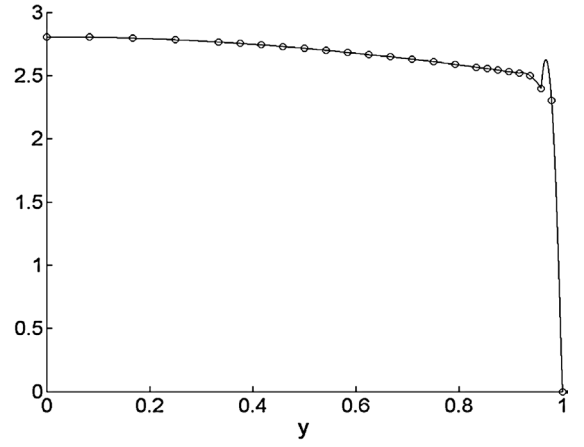

Fig. 15. u_1 on the line $x = 12$. Case 3.2.2. Mesh $\mathcal{M}_1$, $a = 1$, $We = 8\lambda = 1$, $\alpha = 1$, $\theta = \frac{5}{6}$, $\delta = \frac{1}{5}$, $c = \frac{1}{4}$, $\mu = 2$.

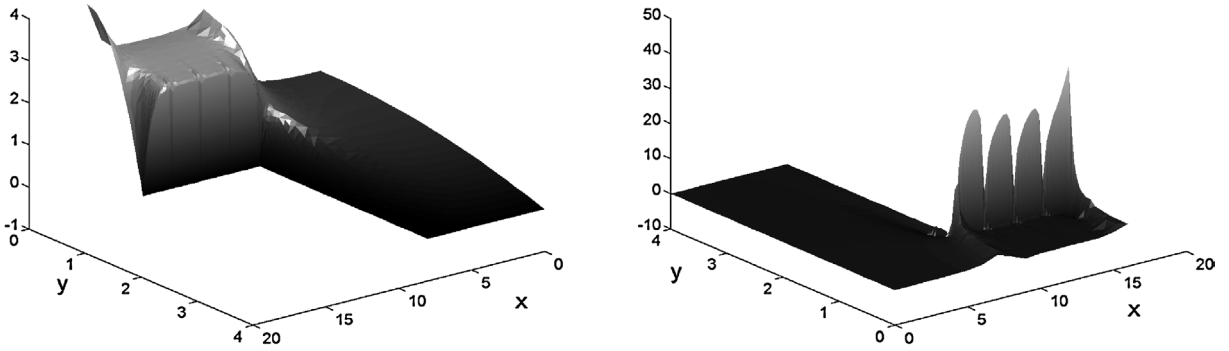

Fig. 16. Graph of u_1 (reverse angle) and σ_{11}. Case 3.2.2 (continuation). Mesh $\mathcal{M}_1$, $a = 1$, $We = 8\lambda = 1$, $\alpha = 1$, $\theta = \frac{5}{6}$, $\delta = \frac{1}{5}$, $c = \frac{1}{4}$, $\mu = 2$.

the tensor σ_{11} gives, on the wall $y = 1$, four oscillations in a thin layer formed of triangles which are adjacent to this wall. We notice that these oscillations correspond to the geometry of the mesh. We take the view that this fact is also due to the three small irregularities on u which appear at this boundary (see Fig. 16). Furthermore, at the beginning of the iterative process, it seems that the method does not converge (see Fig. 14). For this reason and in view of the appearance of σ_{11}, we have often interrupted our computations before convergence. In view of the results of the corotational model we have taken it up again. This is one of our motivations to work with the corotational model.

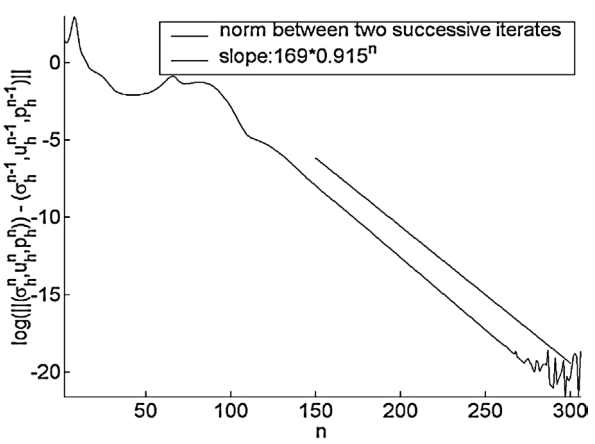

Fig. 17. Ratio of convergence. Case 3.3.1. Mesh $\mathcal{M}_2$, $a = 0$, $We = 8\lambda = 1$, $\alpha = 1$, $\theta = \frac{5}{6}$, $\delta = \frac{1}{5}$, $c = 0$, $\mu = 2$.

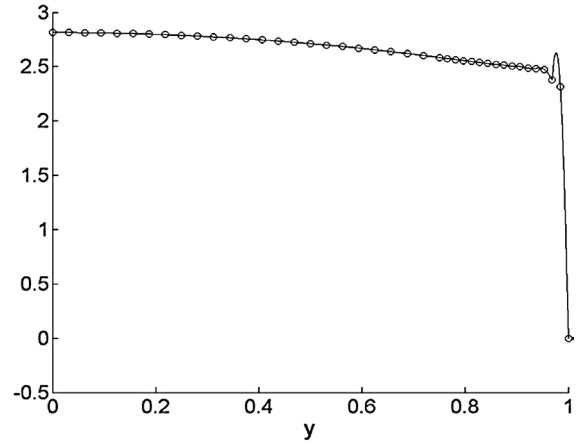

Fig. 18. u_1 on the line $x = 12.16$. Case 3.3.1. Mesh $\mathcal{M}_2$, $a = 0$, $We = 8\lambda = 1$, $\alpha = 1$, $\theta = \frac{5}{6}$, $\delta = \frac{1}{5}$, $c = 0$, $\mu = 2$.

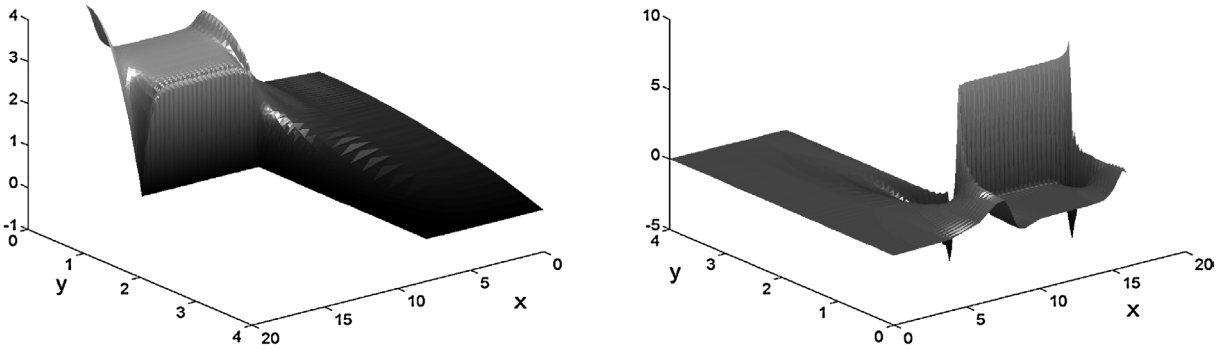

Fig. 19. Graph of u_1 (reverse angle) and σ_{11}. Case 3.3.1 (continuation). Mesh $\mathcal{M}_2$, $a = 0$, $We = 8\lambda = 1$, $\alpha = 1$, $\theta = \frac{5}{6}$, $\delta = \frac{1}{5}$, $c = 0$, $\mu = 2$.

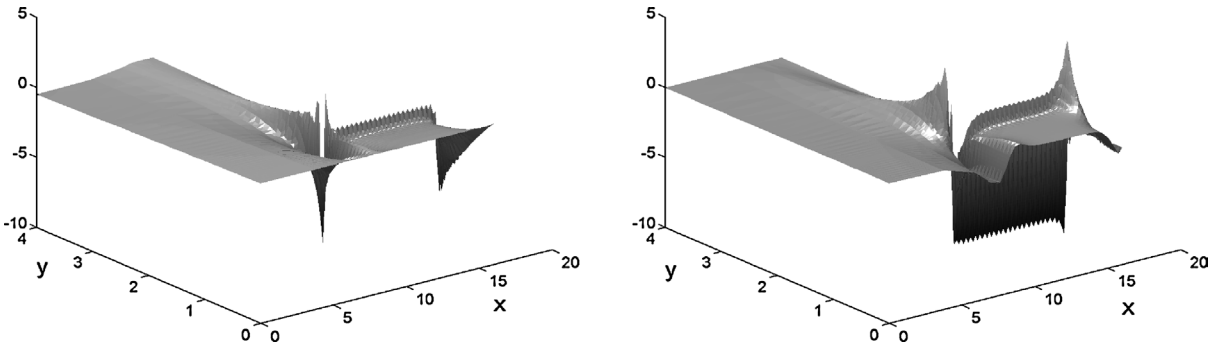

Fig. 19a. Graph of σ_{12} and σ_{22}. Case 3.3.1 (continuation). Mesh $\mathcal{M}_2$, $a = 0$, $We = 8\lambda = 1$, $\alpha = 1$, $\theta = \frac{5}{6}$, $\delta = \frac{1}{5}$, $c = 0$, $\mu = 2$.

3.3. Simulations with the mesh $\mathcal{M}_2$

In view of studying the properties of the FE method and the FE solutions according to the refinement mesh, we use a thinner mesh $\mathcal{M}_2$. In particular, we have tried to verify that the irregularities of σ_{11} at the downstream of the wall (see Fig. 10 and especially Fig. 16) are due for the most part to the irregularities of the mesh. For the mesh $\mathcal{M}_2$ the three following cases are studied:

- Case 3.3.1: $a = 0$, $We = 8\lambda = 1$ with $\alpha = 1$, and the parameters $\delta = \frac{1}{5}$, $\theta = \frac{5}{6}$ and $c = 0$ (Figs. 17–19, 19a).

- Case 3.3.2: $a = 1$, $We = 8\lambda = 1$ with $\alpha = 1$, with the parameters $\delta = \frac{1}{5}$, $\theta = \frac{5}{6}$ and $c = \frac{1}{4}$ (Figs. 20–22).
- Case 3.3.3: as in the case 3.2.2, with $\delta = 1$ in place of $\delta = \frac{1}{5}$ in view of trying to suppress partially the oscillations on σ_{11} of the preceding case (Figs. 23–27).

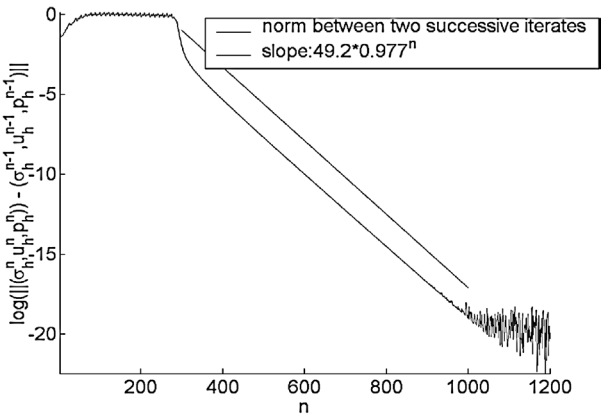

Fig. 20. Ratio of convergence. Case 3.3.2. Mesh $\mathcal{M}_2$, $a = 1$, $We = 8\lambda = 1$, $\alpha = 1$, $\theta = \frac{5}{6}$, $\delta = \frac{1}{5}$, $c = \frac{1}{4}$, $\mu = 2$.

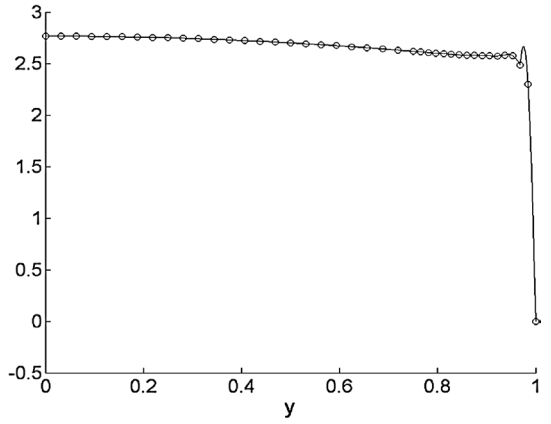

Fig. 21. u_1 on the line $x = 12.16$. Case 3.3.2. Mesh $\mathcal{M}_2$, $a = 1$, $We = 8\lambda = 1$, $\alpha = 1$, $\theta = \frac{5}{6}$, $\delta = \frac{1}{5}$, $c = \frac{1}{4}$, $\mu = 2$.

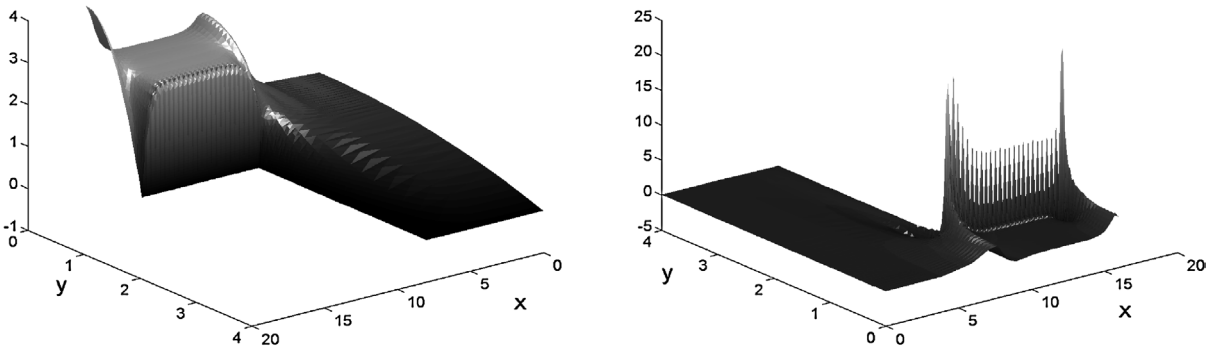

Fig. 22. Graph of u_1 (reverse angle) and σ_{11}. Case 3.3.2 (continuation). Mesh $\mathcal{M}_2$, $a = 1$, $We = 8\lambda = 1$, $\alpha = 1$, $\theta = \frac{5}{6}$, $\delta = \frac{1}{5}$, $c = \frac{1}{4}$, $\mu = 2$.

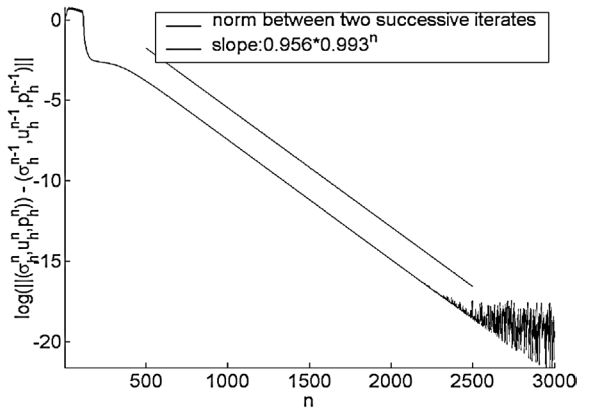

Fig. 23. Ratio of convergence. Case 3.3.3. Mesh $\mathcal{M}_2$, $a = 1$, $We = 8\lambda = 1$, $\alpha = 1$, $\theta = \frac{1}{2}$, $\delta = 1$, $c = \frac{1}{4}$, $\mu = 2$.

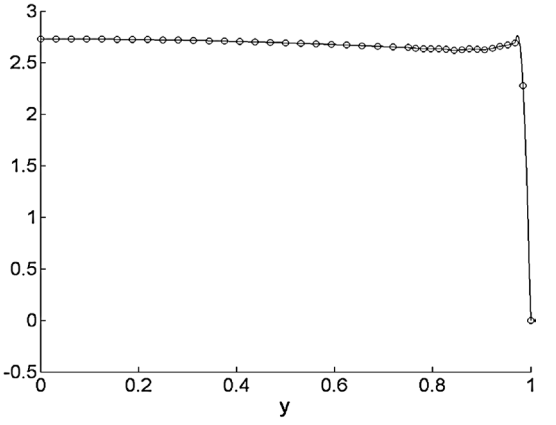

Fig. 24. u_1 on the line $x = 12.16$. Case 3.3.3. Mesh $\mathcal{M}_2$, $a = 1$, $We = 8\lambda = 1$, $\alpha = 1$, $\theta = \frac{1}{2}$, $\delta = 1$, $c = \frac{1}{4}$, $\mu = 2$.

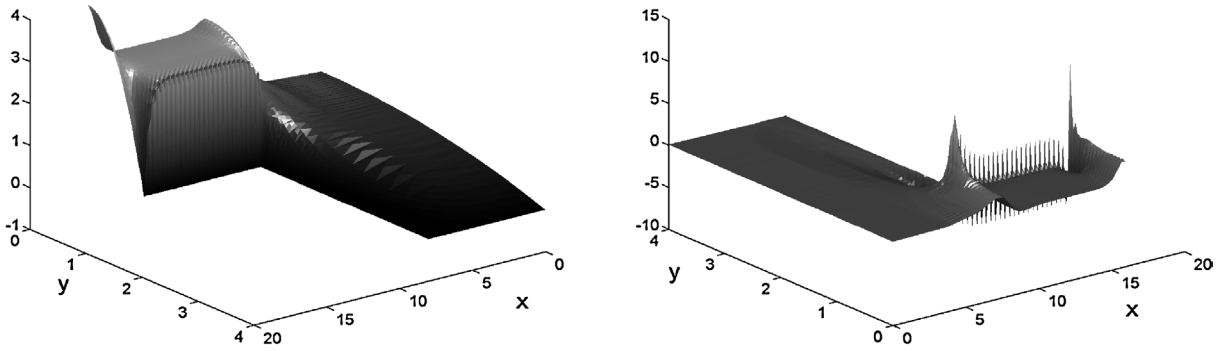

Fig. 25. Graph of u_1 (reverse angle) and σ_{11}. Case 3.3.3 (continuation). Mesh $\mathcal{M}_2$, $a = 1$, $We = 8\lambda = 1$, $\alpha = 1$, $\theta = \frac{1}{2}$, $\delta = 1$, $c = \frac{1}{4}$, $\mu = 2$.

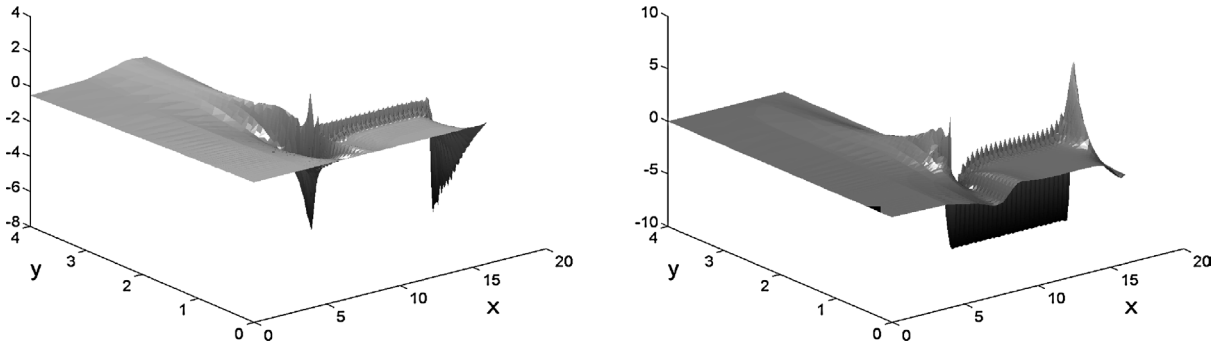

Fig. 25a. Graph of σ_{12} and σ_{22}. Case 3.3.3 (continuation). Mesh $\mathcal{M}_2$, $a = 1$, $We = 8\lambda = 1$, $\alpha = 1$, $\theta = \frac{1}{2}$, $\delta = 1$, $c = \frac{1}{4}$, $\mu = 2$.

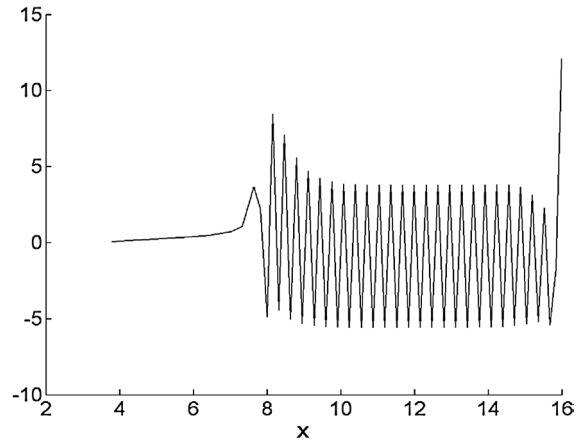

Fig. 26. σ_{11} on the line $y = 1$. Case 3.3.3 (continuation). Mesh $\mathcal{M}_2$, $a = 1$, $We = 8\lambda = 1$, $\alpha = 1$, $\theta = \frac{1}{2}$, $\delta = 1$, $c = \frac{1}{4}$, $\mu = 2$.

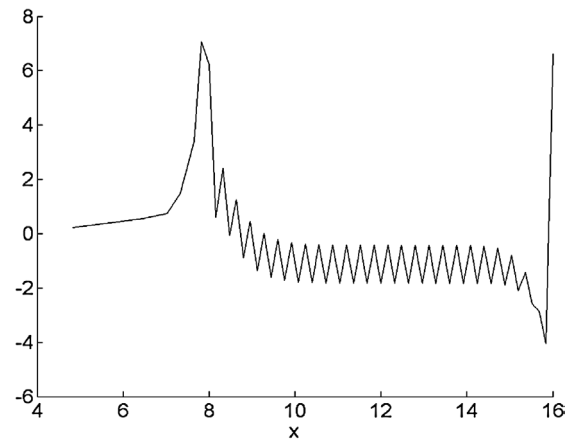

Fig. 26a. σ_{11} on the line $y = 0.96875$. Case 3.3.3 (continuation). Mesh $\mathcal{M}_2$, $a = 1$, $We = 8\lambda = 1$, $\alpha = 1$, $\theta = \frac{1}{2}$, $\delta = 1$, $c = \frac{1}{4}$, $\mu = 2$.

Results are summarized in Figs. 17–27. Generally, for the upper-convected Oldroyd-B model, the ratio of convergence of the iterative methods used to solve the approximate problem increases with the refinement of the mesh (see for example [5]), this is also the case for the method of this paper in the case of "embedded meshes" (see [4]). Nevertheless, if we compare the simulations of Figs. 8 and 17 (corotational case) and of Figs. 14 and 20 (upper convected case), we see that, with the mesh $\mathcal{M}_2$, the ratio of convergence of the method remains of the same order with, in the corotational case, an important improvement in relation to the mesh $\mathcal{M}_1$. We think that this is due to the fact that the mesh $\mathcal{M}_2$ and the approximated solutions are more

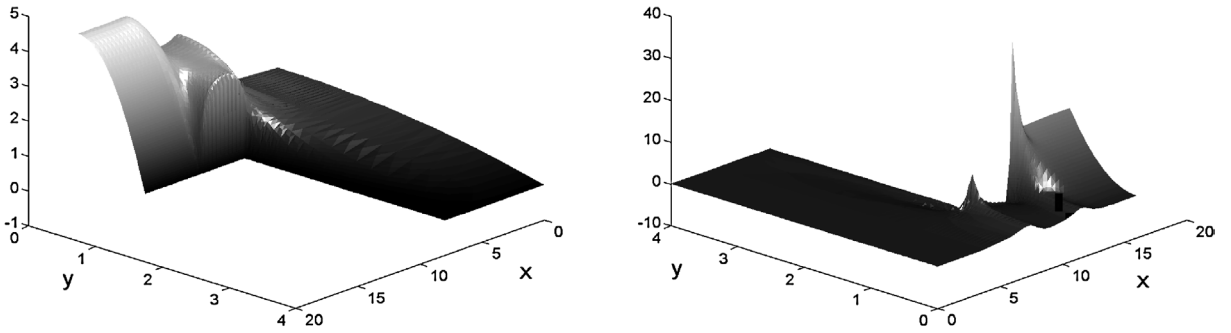

Fig. 27. Graph of u_1 (reverse angle) and σ_{11}. Case 3.3.3 (continuation). Mesh $\mathcal{M}_2$, iterate number 52, $a = 1$, $We = 8\lambda = 1$, $\alpha = 1$, $\theta = \frac{1}{2}$, $\delta = 1$, $c = \frac{1}{4}$, $\mu = 2$.

regular in the downstream section. Furthermore, in the corotational case, we take the view that the properties coming from (1.1) participate to the improvement of the ratio of convergence.

For the corotational model, the results are close to those obtained with the mesh $\mathcal{M}_1$. We remark, comparing Figs. 10 and 19, that for the corotational model the small irregularities of Fig. 10 vanish. The phenomenon of quasi-slip on the velocity increases slightly with the thinner mesh $\mathcal{M}_2$. Indeed, on Fig. 18, u_1 has the value $u_1(12.16, 0.96875) = 2.38$ and for the degree of freedom just before the wall $u_1(12.16, 0.984375) = 2.32$, this point being closer of the wall than the corresponding point of Fig. 9.

In Fig. 19a, we have plotted the components σ_{12} and σ_{22} of the tensor σ.

Now, let us consider the case 3.3.2 devoted to the upper convected model. In Fig. 21, the values $u_1(12.16, 0.96875) = 2.49$ and $u_1(12.16, 0.984375) = 2.30$ indicate again, in relation to Fig. 15, a slight increase in the quasi-slip phenomenon. In Fig. 22, in comparison with Fig. 16, we see that the magnitude of the oscillations of σ_{11} decreases with the thinner mesh $\mathcal{M}_2$.

In the third case 3.3.3 we recover again, in Fig. 24, high values for u_1 near the wall: $u_1(12.16, 0.96875) = 2.69$ and $u_1(12.16, 0.984375) = 2.28$. For this case, the magnitude of the oscillations of σ_{11} still decreases with the choice of $\delta = 1$ (see Fig. 25).

In Fig. 25a, we have plotted the components σ_{12} and σ_{22} of the tensor σ. We note that the oscillations are of very smaller magnitude than in the σ_{11} case.

In Figs. 26 and 26a we have plotted the graphics of σ_{11} at the wall $y = 1$ and near this wall. The magnitude of the oscillations decreases quickly in Fig. 26a, and we notice that the strip which contains the most important part of the oscillations is relatively narrow. From the examination of Figs. 22, 25, 26 and 26a, it seems that we have at least L^1-convergence of σ_{11h} towards a solution σ_{11} composed of two peaks located at the re-entrant corner and at the outflow boundary.

In Fig. 27, we represent the results obtained at the iterate number 52. We see that, in the iterative process, there is a propagation along the wall $y = 1$ of the peak of σ_{11} and of the quasi-slip of u_1.

To end the simulations of this section, we present in Figs. 28–30 a simulation of the upper convected Maxwell model with higher Weissenberg number. Now, in this simulation, there appears a second singularity at the downstream for $x \geqslant 12.3$ and $y_1' \simeq 0.96875$ (as if the flow selects two solutions in a continuum of solution). In the graph of Fig. 31 we see that the component u_1 is almost null on a thin layer adjacent to the wall $y = 1$. In the same way the velocity is also almost null on this layer.

3.4. Discussion about the numerical results

Let us now discuss the appearance of the quasi-slip in the above simulations. For that, we study the relationship between the plane Poiseuille flow, the numerical simulations for a flow through a rectangle and the results obtained in the case of the contraction 4 to 1. Let us consider the Oldroyd problem in the case of a Poiseuille type flow first. We consider a fluid flowing in the domain $\Omega_2 =]-\infty, +\infty[\times]-1, 1[$. We assume that the flow is laminar, moving in the $+x$ direction and satisfies the Oldroyd problem:

$$(\mathcal{P}_2) \quad \begin{cases} \sigma + \lambda B(u, \sigma) = 2\alpha d(u) & \text{in } \Omega_2, \\ -\nabla \cdot \sigma - 2(1-\alpha)\nabla \cdot d(u) + \nabla p = 0 & \text{in } \Omega_2, \\ \nabla \cdot u = 0 \quad \text{in } \Omega_2, \\ u(x, -1) = u(x, 1) = 0, \quad \forall x \in \mathbb{R}. \end{cases}$$

Furthermore, we assume that the pressure gradient in the flow direction $p_{,1}$ is a negative constant and that the tensor σ depends only on y. In the sequel we denote by $u^\star$ the velocity solution for this Poiseuille type flow and we set $f = -p_{,1} \geqslant 0$ and $k = \lambda\sqrt{1-a^2}$. We have the following existence result (see, for example, [6], Eq. (2.8) and Proposition 2.1):

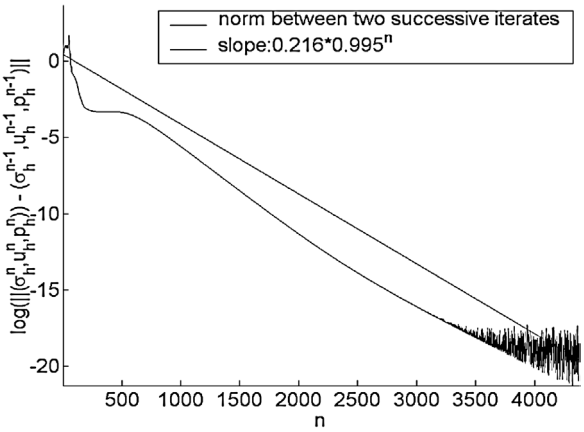

Fig. 28. Ratio of convergence. Mesh $\mathcal{M}_2$, $a = 1$, $We = 8\lambda = 1.2$, $\alpha = 1$, $\theta = \frac{1}{2}$, $\delta = 1$, $c = \frac{1}{4}$, $\mu = 2$.

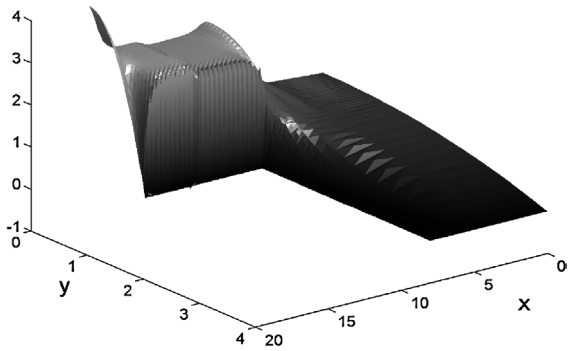

Fig. 29. u_1. Mesh $\mathcal{M}_2$, $a = 1$, $We = 8\lambda = 1.2$, $\alpha = 1$, $\theta = \frac{1}{2}$, $\delta = 1$, $c = \frac{1}{4}$, $\mu = 2$.

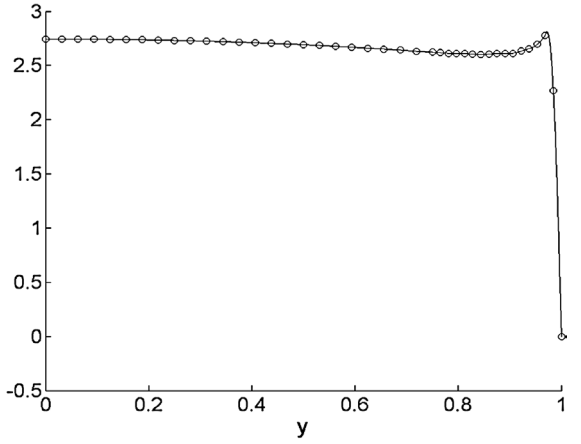

Fig. 30. u_1 on the line $x = 12.16$. Mesh $\mathcal{M}_2$, $a = 1$, $We = 8\lambda = 1.2$, $\alpha = 1$, $\theta = \frac{1}{2}$, $\delta = 1$, $c = \frac{1}{4}$, $\mu = 2$. We have $u_1(12.16, 0.96875) = 2.78$, $u_1(12.16, 0.984375) = 2.27$.

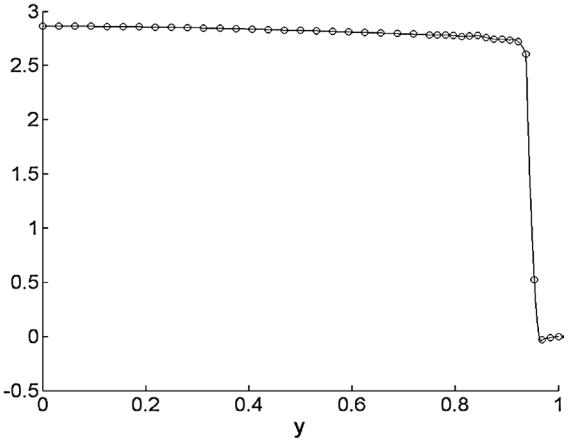

Fig. 31. u_1 on the line $x = 14.08$. Mesh $\mathcal{M}_2$, $a = 1$, $We = 8\lambda = 1.2$, $\alpha = 1$, $\theta = \frac{1}{2}$, $\delta = 1$, $c = \frac{1}{4}$, $\mu = 2$. We have $u_1(14.08, 0.96875) = -0.03$, $u_1(14.08, 0.984375) = -0.01$.

- Case 3.4.1. Let $|a| = 1$ and $\alpha \in [0, 1]$. There exists a unique $\mathcal{C}^1$ Poiseuille flow $u^\star$ given by

$$u_1^\star(x, y) = \frac{f}{2}(1 - y^2), \qquad u_2^\star(x, y) = 0. \tag{3.1}$$

- Case 3.4.2. Let $a \in]-1, 1[$ and $\alpha = 1$. If $f \leqslant f_c$, with $f_c = \frac{1}{2k}$, then there exists a unique $\mathcal{C}^1$ Poiseuille flow $u^\star$ given by

$$u_1^\star(x, y) = \int_1^y \frac{-2fs}{1 + \sqrt{1 - 4f^2k^2s^2}}\,\mathrm{d}s, \qquad u_2^\star(x, y) = 0. \tag{3.2}$$

- Case 3.4.3. Let $a \in]-1, 1[$ and $\alpha < 1$.
  (a) Let $\alpha \in [0, \frac{8}{9}]$. There exists a unique $\mathcal{C}^1$ Poiseuille flow.
  (b) Let $\alpha \in]\frac{8}{9}, 1[$. There exists some critical $f_c^\alpha > 0$ such that:
    (i) if $f \leqslant f_c^\alpha$, then there exists a unique $\mathcal{C}^1$ Poiseuille flow,

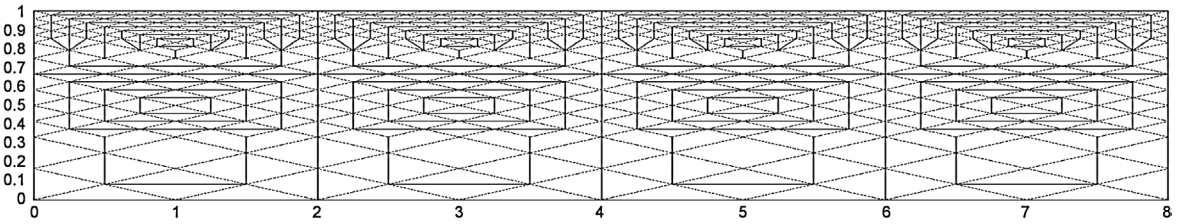

Fig. 32. Mesh $\mathcal{M}_3$.

(ii) if $f > f_c^\alpha$, then there does not exist a $\mathcal{C}^1$ Poiseuille flow, but there exists a continuum of $\mathcal{C}^0$ flows which are $\mathcal{C}^\infty$ except on two lines $y = \tilde{y}$ and $y = -\tilde{y}$, with $\tilde{y} \in]0, 1[$, across which $u^\star_{1,2}$ presents a jump. The critical value f_c^α is given by

$$f_c^\alpha = \gamma_-^\alpha \frac{1 + (1-\alpha)(k\gamma_-^\alpha)^2}{1 + (k\gamma_-^\alpha)^2}, \quad \text{with } \gamma_\pm^\alpha = \frac{1}{k}\left(\frac{3\alpha - 2 \pm \sqrt{\alpha(9\alpha - 8)}}{2(1-\alpha)}\right)^{1/2} \tag{3.3}$$

and $\tilde{y}$ is located in $[y_+, y_-] \subset]0, 1[$ with

$$y_\pm = \frac{\gamma_\pm^\alpha}{f} \frac{1 + (1-\alpha)(k\gamma_\pm^\alpha)^2}{1 + (k\gamma_\pm^\alpha)^2}. \tag{3.4}$$

Now, in order to compare the Poiseuille flow and the flow in the downstream section of the contraction 4 to 1, we first have studied numerically the case of a flow through a rectangle $Q = [0, 1] \times [0, 8]$, with Q corresponding to the downstream section of the contraction 4 to 1 (in view of the symmetry of the flow we use Q in place of $[-1, 1] \times [0, 8]$). We have chosen Newtonian Poiseuille flow at the inflow boundary and Neumann condition at the outflow boundary. The problem considered in Q is the following:

$$(\mathcal{P}_3) \quad \begin{cases} \sigma + \lambda B(u, \sigma) = 2\alpha d(u) & \text{in } Q, \\ -\nabla \cdot \sigma - 2(1-\alpha)\nabla \cdot d(u) + \nabla p = 0 & \text{in } Q, \\ \nabla \cdot u = 0 & \text{in } Q, \end{cases}$$

with the following boundary conditions:

- at the inflow boundary $x = 0$ and $y \in [0, 1]$: $u_1(0, y) = 4(1 - y^2)$, $u_2(0, y) = 0$ and $\sigma = 2\alpha d(u)$,
- at the outflow boundary $x = 8$ and $y \in [0, 1]$: either $(\sigma_{\text{tot}} \cdot n) \cdot t = 0$ and $u_2 = 0$ (fully developed profile) or $(\sigma_{\text{tot}} \cdot n) = 0$ where $\sigma_{\text{tot}} = (\sigma + 2(1-\alpha)d(u) - pI)$ (we present results obtained with the second condition; however, except at the exit of the channel, computations show that both conditions give similar solutions),
- at the wall $x \in [0, 8]$ and $y = 1$: $u_1(x, 1) = u_2(x, 1) = 0$,
- at the boundary $x \in [0, 8]$ and $y = 0$ (symmetry): $u_2 = 0$, $(\sigma_{\text{tot}} \cdot n) \cdot t = 0$.

With these inflow boundary conditions we have the same volume rate of flow than in the contraction case. We notice that, with these boundary conditions, the problem $(\mathcal{P}_3)$ appears as a perturbation of the plane Poiseuille flow.

Computations are made on a mesh $\mathcal{M}_3$ (see Fig. 32) which corresponds to the mesh $\mathcal{M}_1$ in the downstream section of the contraction 4 to 1. In this section, all the computations on $(\mathcal{P}_3)$ are made with $c = 0$ for $|a| < 1$ and $c = 1/4$ for $|a| = 1$. We have used $\delta = 1/5$ and $\delta = 1/10$ with similar results. Comparisons with the contraction 4 to 1 are made with the results obtained on the mesh $\mathcal{M}_1$, with $c = 0$ for $|a| < 1$ and $c = 1/4$ for $|a| = 1$ and with $\delta = 1/5$.

Now, we compare $u^\star$ and u_Q, where u_Q is the velocity solution of $(\mathcal{P}_3)$.

3.4.1. The case $\alpha = 1$. Simulations on the rectangle Q

Let us examine the case $\alpha = 1$ (cases 3.4.1 and 3.4.2 above). The conservation of the volume rate of flow gives the corresponding value of f in $u^\star$ given by Eq. (3.1-2). Then f has to satisfy (we set $f_c = +\infty$ for $|a| = 1$):

$\exists f \leqslant f_c$ *such that*:

$$\int_{-1}^{1} u_1^\star(x, y)\, dy = \int_{-1}^{1} 4(1 - y^2)\, dy = \frac{16}{3}, \quad \textit{with } u^\star \textit{ given by } (3.1) \textit{ or } (3.2). \tag{3.5}$$

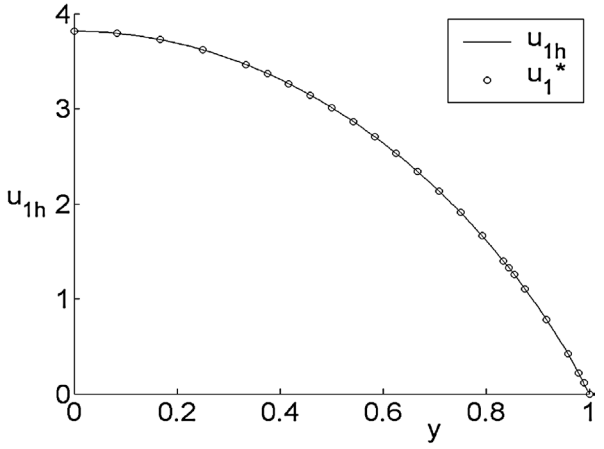

Fig. 33. u_1 on the line $x = 4$ for $a = 0$, $\alpha = 1$ and $We = 8\lambda = 0.64$. —: Approximated solution on the mesh $\mathcal{M}_3$ with $\theta = \frac{10}{11}$, $\delta = \frac{1}{10}$, $c = 0$, $\mu = 2$. o: Exact Poiseuille flow given by (3.2) with $f = 6.235$.

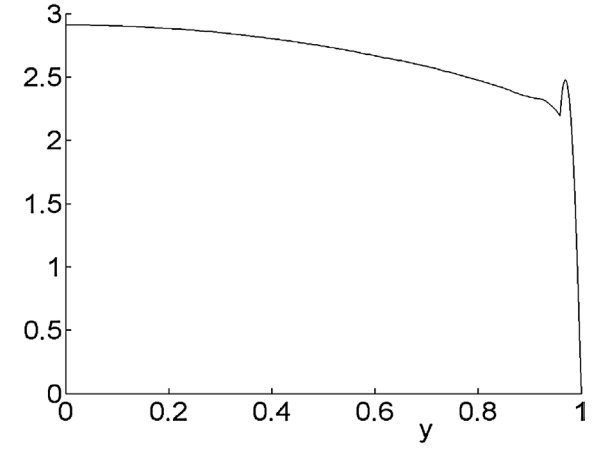

Fig. 34. Approximated solution of $(\mathcal{P}_3)$: u_1 on the line $x = 4$ for $a = 0$, $\alpha = 1$ and $We = 8\lambda = 0.66$. Mesh $\mathcal{M}_3$, $\theta = \frac{10}{11}$, $\delta = \frac{1}{10}$, $c = 0$, $\mu = 2$.

For $|a| = 1$, Eq. (3.5) gives $f = 8$ in (3.1). For $|a| < 1$, a numerical study shows that Eq. (3.5), with $u^\star$ given by (3.2), has a unique solution f if and only if $k = \lambda\sqrt{1 - a^2}$ satisfies:

$$k \leqslant k_c \quad \text{where } k_c \simeq 0.0805. \tag{3.6}$$

We can see in the numerical tests below that the quasi-slip appears in the rectangle Q when $k = \lambda\sqrt{1 - a^2}$ becomes greater than k_c. For $a = 0$, Eq. (3.6) gives the condition $k = \lambda \leqslant 0.0805$ i.e. $We = 8\lambda \leqslant 0.6440$. We have made simulations around this value. Let us consider the case $a = 0$ and $We = 0.64$. For these values the solution of (3.5) is then given by $f \simeq 6.235$. Using this value of $f = 6.235$ for $u^\star$ in (3.2) we find that $|u_{Qh} - u^\star| \leqslant 0.0075$ in $[2, 6] \times [0, 1]$ where u_{Qh} is the approximate solution of u_Q (see Fig. 33). In this way we see that $u^\star$ is stable for u_Q. Now, for $We = 0.66$ (for this case (3.5) has no solution $u^\star$ given by (3.2)) we see that a quasi-slip appears in the domain Q (see Fig. 34).

More generally, we have noticed that for $We \leqslant 0.64$, $u^\star$ remains stable for u_Q while for $We \geqslant 0.66$ the quasi-slip appears (tests performed up to $We = 1.2$). We have also observed this phenomenon for other values of a such as $a = 0.4$ and $a = 0.8$ with the corresponding critical values given by (3.6): $We \simeq 0.7027$ and $We \simeq 1.0733$. Now, for $|a| = 1$ ((3.5) is then always satisfied with $f = 8$ in (3.1)) the quasi-slip does not appear when We increases and $u^\star$ remains stable for u_Q (tests performed up to $We = 1.4$ for $a = 1$). In conclusion, it appears that for $k \lesssim k_c$ (including the case $|a| = 1$) the solution u_Q stabilizes towards the Poiseuille flow while a quasi-slip appears for $a \in]-1, 1[$ (with $\alpha = 1$), when (3.5) can not be satisfied, i.e. for $k \gtrsim k_c$.

3.4.2. The case $\alpha = 1$. Simulations on the contraction 4 to 1

Now, let us consider the flow through the second part of the channel of the contraction 4 to 1 (always with $\alpha = 1$). For $a = 0$ the solution stabilizes towards the Poiseuille flow but only for $We \leqslant 0.59$ instead of $We \leqslant 0.64$ in the case of the rectangle. Then, starting from $We = 0.60$ a quasi-slip appears along the wall. In the iterative process, this quasi-slip appears progressively, by propagation as in Fig. 27. This propagation effect disappears progressively when We increases. We get a similar behaviour for $a = 0.4$ (resp. $a = 0.8$) with the following critical values for the appearance of the quasi-slip: $We = 0.64$ (resp. $We = 0.82$) instead of $We = 0.72$ (resp. $We = 1.09$) in the case of the rectangle. Finally, for $a = 1$ and in contrast to the rectangle Q, the quasi-slip appears also starting from $We \geqslant 0.95$. Similar results are obtained for $a < 0$. In this way it appears in all cases $a = 0$, 0.4, 0.8, 1, that a second mechanism contributes to the quasi-slip at the wall. We think that this mechanism is due to the singularity of the flow located at the corner. In order to study the influence of the FEM on this mechanism, we have used in problem $(\mathcal{Q}_h)$ the more classic $\delta\lambda u_h \cdot \nabla\tau$ term instead of $\delta\lambda B(u_h, \tau)$. With this term, for $|a| < 1$, it appears that the phenomenon persists but is less important. Indeed, the critical values for the appearance of the quasi-slip increase: $We = 0.61$ for $a = 0$, $We = 0.66$ for $a = 0.4$ and $We = 1.01$ for $a = 0.8$ while for $a = 1$ the quasi-slip disappears. In this way, the appearance of quasi-slip for $k < k_c$, especially when we have $|a| = 1$, remains an open problem. Concerning the flow in the first part of the channel, the corresponding Weissenberg number is given by $We' = |u_{1,2}(0, 4)| = 16We$. In this way we see that the Weissenberg numbers used in our computations are too small to produce a quasi-slip effect in this part of the channel. On the other hand, for a channel of width 8 instead of 2, we can check that the corresponding condition (3.6) becomes $k \leqslant 16k_c$. For example, for $a = 0$, this gives $We \simeq 10.64$. Computations on a rectangle of width 4 instead of 1 show that quasi-slip arises around this value of We.

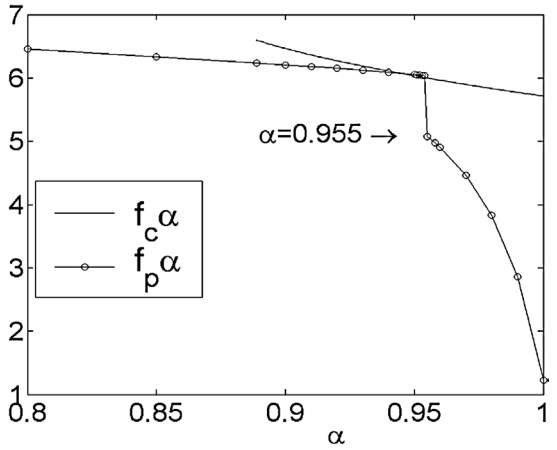

Fig. 35. Plots of f_c^α vs. α, $\frac{8}{9} \leqslant \alpha \leqslant 1$ (see Eq. (3.3)) and f_p^α vs. α, $0.8 \leqslant \alpha \leqslant 1$. $a = 0$, $\lambda = 0.0875$.

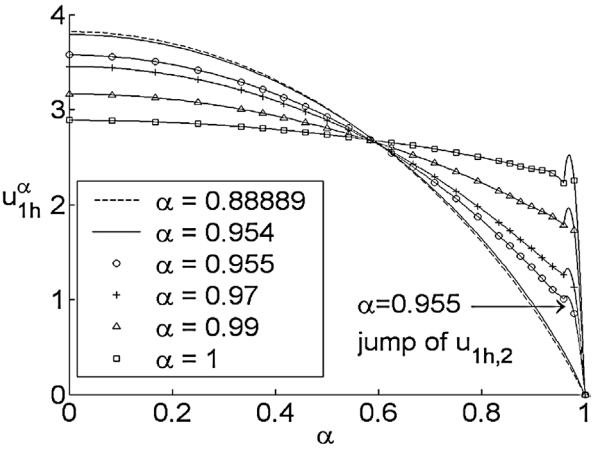

Fig. 36. Approximate solution of u_1 on the line $x = 4$. Mesh $\mathcal{M}_3$, $a = 0$, $We = 8\lambda = 0.7$, $\theta = \frac{10}{11}$, $\delta = 1/10$, $c = 0$, $\mu = 2$.

3.4.3. The case $\alpha < 1$. Simulations on the rectangle Q

Now, let us examine the case $\alpha \in]0, 1[$ (see case 3.4.3), particularly when α tends to 1. We present numerical results obtained in Q, for $a = 0$, $\alpha \in]0.8, 1[$ and $\lambda = 0.0875$, i.e. $We = 0.7$. This value of We is chosen in order to have, for $\alpha = 1$, a quasi-slip at the wall (see Section 3.4.1). Let $\alpha \in [0, 1]$, we denote by p_h^α the approximate pressure. In our simulations, we have noticed that $p_{h,1}^\alpha$ remains approximately constant on $[2, 6] \times [0, 1]$. We denote by f_p^α the mean value of $-p_{h,1}^\alpha$ on this rectangle. In Fig. 35, we have plotted f_c^α given by (3.3) and f_p^α versus α. When α increases, it appears that the difference $f_c^\alpha - f_p^\alpha$ decreases and becomes negative: we obtain $f_p^\alpha > f_c^\alpha$ for $\alpha \in [0.945, 0.954]$ (see Fig. 35). In the Poiseuille flow case, this corresponds to the case $f > f_c^\alpha$, with the appearance of a continuum of solutions whose singularity is located on a line $y = \tilde{y}$, with $\tilde{y} \in [y_+, y_-]$ (see case 3.4.3(ii)). We notice that $\lim_{f \to f_c^{\alpha+}} y_- = 1$, thus, for $f \simeq f_c^\alpha$ (with $f > f_c^\alpha$), a solution exists with a singularity close to the wall. In the case of the rectangle, we see that the case $f_p^\alpha > f_c^\alpha$ corresponds, from $\alpha = 0.955$, to the appearance of a solution with a singularity of the same kind: $u_{1h,2}(x, y)$ presents a jump on a line $y = \tilde{y}$ close to 1 (see Fig. 36). Furthermore, we see in Fig. 35 that f_p^α drops roughly with $f_p^\alpha < f_c^\alpha$. Next, when α increases up to 1, we see that the solutions remain singular and tend towards the solution obtained for $\alpha = 1$, with a quasi-slip at the wall (see Fig. 36).

In this way, when α tends to 1, we see that the solutions with quasi-slip at the wall appear as the limit of solutions whose singularity is located on parallel lines to the wall and close to it. We have also observed this phenomenon for other values of $a \in]-1, 1[$ and $k = \lambda\sqrt{1 - a^2} > k_c$. However, for $|a| = 1$, as in the Poiseuille flow case, the flow remains regular (tests performed up to $We = 1.4$ for $a = 1$).

3.4.4. The case $\alpha < 1$. Simulations on the contraction 4 to 1

In the case of the contraction 4 to 1, for $a = 0$ and $\lambda = 0.0875$, we obtain a phenomenon which is comparable to the phenomenon described in Figs. 35 and 36: $f_c^\alpha - f_p^\alpha$ decreases towards 0 first, with a minimal value given by $f_c^\alpha - f_p^\alpha = 0.0748$ for $\alpha = 0.929$, then, f_p^α drops roughly for $\alpha = 0.93$, with the appearance of a singular solution. Thus, singular solutions arise for smaller values of α than in the case of the rectangle. Moreover, a propagation of the singularity arises in the iterative process. We obtain a similar phenomenon for $a = 1$: for $We = 1$, f_p^α drops from $\alpha \simeq 0.995$ with the appearance of a singular solution. As for $a = 1$ and $\alpha = 1$, this phenomenon disappears for $a = 1$ and $\alpha < 1$, when we choose in problem $(\mathcal{Q}_h)$ the $\delta\lambda u_h.\nabla\tau$ term instead of $\delta\lambda B(u_h, \tau)$ and $\theta = 1$ instead of $\theta = \frac{1}{1+\delta}$ (in this case we recognize a classical method for the simulation of viscoelastic flows, we recall that this method is not available for $\alpha = 1$). And to conclude, for $|a| < 1$ and for λ sufficiently high, there appears a breaking value of α for which, similarly to the Poiseuille flow case, the derivative $u_{1h,2}$ presents a jump across a parallel line to the wall and close to it. Furthermore, when α tends to 1, the solution with quasi-slip (with $\alpha = 1$) appears as the limit of the solutions obtained for $\alpha < 1$. Unlike the Poiseuille flow case, this phenomenon also persists for $|a| = 1$, but it is sensitive to the FEM used (tests performed for $We = 1$). Thus, for $|a| = 1$, the quasi-slip is more puzzling and it seems, even more than for $|a| < 1$, that the singularity at the corner plays an important part in the appearance of the quasi-slip. We notice that the breaking value of α is located in $[\frac{8}{9}, 1[$ and depends on a and λ.

4. Conclusion

Let us consider the case of the contraction 4 to 1. When the quasi-slip appears, the corotational model gives at the downstream wall numerical solutions which are more regular than the solutions obtained with the upper convected model for which oscillations on σ appears (see the component σ_{11} of the tensor σ in Figs. 10, 16, 19, 22 and 25). The corotational model (and more generally the case $|a| < 1$) indicates the possibility of the existence of a phenomenon of quasi-slip near the boundary for a sufficiently high Weissenberg number (from $We = 0.6$, for $a = 0$, in our simulations). This possibility is reinforced by the analysis on the Poiseuille flow. In the upper convected case, although the tensor σ_{11} gives oscillations which can spoil the quality of the results, it seems, in view of the corotational model, that this phenomenon of quasi-slip is not due to the difficulties which arise in the approximation of σ_{11}. As in Fig. 16, we have noticed in some other simulations, and notably for the upper convected model, that the results depend on the quality of the mesh. However, in the upper convected model case, in order to study the Poiseuille flow (in the upper convected model case, the solution of the plane Poiseuille flow exists and is regular for all $\lambda > 0$), the existence of a quasi-slip at the downstream wall of the contraction remains an open question, in particular, it seems that the singularity located at the corner could play an important part in this phenomenon (as well as for $|a| < 1$).

As far as we know, in relation to a fluid flowing in a contraction, we have not found this quasi-slip in the literature. There are some hypotheses to explain the difficulties encountered in the simulations to obtain it. Often, it is the Oldroyd-B model with $\alpha = \frac{8}{9}$ which is considered, whereas in this case we have not observed a quasi-slip. Furthermore, does the choice of the FEM allow to capture this phenomenon, as seen with the use of the $\delta\lambda u_h \cdot \nabla\tau$ term instead of $\delta\lambda B(u_h, \tau)$ in $(\mathcal{Q}_h)$ (case $a = 1$)? The choice of the mesh also plays a significant part in our simulations. Often the meshes are refined only at the corner and not along the wall, furthermore, in the mesh refinement process, the size of the triangles often quickly decreases and this can lead to numerical instabilities, particularly in the convergence of the iterative methods used for the simulations. Finally, in the computational experiments, the computation can be interrupted too soon either because the scheme seems to be diverging at the beginning of the iterative process as in Figs. 14, 20 and 23, or because the solution is oscillating as in Figs. 16, 22 and 25, or before the quasi-slip phenomenon appears. Indeed, during the iterative process, we observe that there is a slow propagation of the quasi-slip from the corner towards the end of the downstream section, as shown in Fig. 27, before obtaining a complete convergence.

Acknowledgements

The author acknowledges the referees for their helpful suggestions. I am most grateful to C. Disaro, English Teacher, for the rereading of the manuscript.

References

[1] R.B. Bird, R.C. Armstrong, O. Hassager, Dynamics of Polymeric Liquids, vols. I & II, Wiley, Amsterdam, 1987.
[2] D. Sandri, On a FEM method for a linearized version of the Oldroyd problem, Comput. Methods Appl. Mech. Engrg. 191 (2002) 5045–5065.
[3] D. Sandri, Sur une méthode d'éléments finis pour les écoulements de polymères, C. R. Acad. Sci. Paris, Ser I 336 (8) (2003) 687–690.
[4] D. Sandri, Numerical study of a new finite element method for the approximation of viscoelastic fluid flow problems, J. Non-Newtonian Fluid Mech. 118 (2004) 103–120.
[5] P. Keunings, in: Ch. Tucker III (Ed.), Computer Modelling for Polymer Processing, Hanser Verlag, Munich, 1989, pp. 403–469.
[6] C. Guillopé, J.-C. Saut, Global existence and one-dimensional non linear stability of shearing motions of viscoelastic fluids of Oldroyd type, Modél. Math. Anal. Numér. 24 (3) (1990) 369–401.